

Article

Fabricating Dispersed Fine Silver Nanoparticles on Liquid Substrate for Improved Photocatalytic Water Splitting Efficiency

Chuhang Zhang 

Department of Physics, Zhejiang University of Science and Technology, Hangzhou 310008, China; 114061@zust.edu.cn; Tel.: +86-137-5086-5421

Abstract: Dispersed silver nanoparticles (NPs) are synthesized on a silicone oil substrate under varied substrate temperature T by thermal vaporization method. Scanning electron microscopic investigation demonstrates that the mean size of the NPs are around 7.8 nm with a standard deviation of 1.0 nm. The NPs are transferred to a strontium titanate (STO) crystal as co-catalyst for water splitting efficiency test. The photoelectrochemical (PEC) measurement reveals the photocatalytic activity of NP co-catalyst sensitively relies on T during deposition process: the relative current density j_r increases from 4.8 $\mu\text{A}/\text{cm}^2$ to 25.4 $\mu\text{A}/\text{cm}^2$ as T goes up from 253 K to 333 K. However, a slight decrease of j_r from 25.4 $\mu\text{A}/\text{cm}^2$ to 22.8 $\mu\text{A}/\text{cm}^2$ is found as T further increases to 353 K. The dependent behavior of j_r on T is explained in term of a competition mechanism between microstructure evolution and growth model of the NPs under different T : for T ranging from 253 K to 333 K, the effect of a higher crystalline structure for NPs fabricated under higher T improves the electron transfer rate from STO to NPs is dominant. As T increases to 353 K, the overlapping of NPs become a factor for photocatalytic activity of NP/STO system: the diffusion distance of electrons becomes larger and the apparent contact area between NPs and STO is reduced which in turn reduce the photocatalytic activity of NP/STO. The experimental method to synthesize NPs in this report may open up a way to further apply fine NPs in enhancing photocatalytic water splitting efficiency.

Keywords: dispersed nanoparticles; crystalline structure; co-catalyst; photocatalytic activity



Citation: Zhang, C. Fabricating Dispersed Fine Silver Nanoparticles on Liquid Substrate for Improved Photocatalytic Water Splitting Efficiency. *Catalysts* **2023**, *13*, 946. <https://doi.org/10.3390/catal13060946>

Academic Editors: Umut Aydemir and Naeimeh Sadat Peighambaroust

Received: 27 April 2023

Revised: 21 May 2023

Accepted: 26 May 2023

Published: 28 May 2023



Copyright: © 2023 by the author. Licensee MDPI, Basel, Switzerland. This article is an open access article distributed under the terms and conditions of the Creative Commons Attribution (CC BY) license (<https://creativecommons.org/licenses/by/4.0/>).

1. Introduction

Fabrication of an efficient photocatalyst toward higher water splitting efficiency has been a critical field since 1972 because it opened up a promising way for cost-efficiency production of sustainable energy of hydrogen [1–3]. Conventional perovskite type semiconductors such as titanium dioxide (TiO_2) and strontium titanate (SrTiO_2) were employed to investigate the mechanism of the photocatalytic water splitting [4,5]. Generally speaking, electrons in valence band of the semiconductors absorb photon from external radiation such as ultraviolet light to overcome the band gap, leaving a hole in the valence band in the meantime. The hydrogen ions in the water or solution capture electrons to become hydrogen while the hole is transferred to the hydroxyl, forming oxygen. Due to the large band gap for conventional semiconductors, they show poor visible light response and low photon to electron conversion efficiency. In order to initiate the visible light absorption, various types of doping were introduced to the semiconductors towards a higher photon to electron conversion efficiency [6,7]. However, introducing impurity energy levels to the semiconductor was less controllable and technically costly.

Due to the unique size-specific effect on nanostructures, various kinds of nanostructure such as nanofiber, nanowire, nanocluster (NC) and quantum dots have been synthesized and decorated on semiconductor as co-catalyst [8–14]. Among them, nanoclusters (NCs) have been extensively utilized as co-catalyst on semiconductor surface to reconstruct the electronic states of the semiconductors. Comparing with the NCs, nanoparticles (NPs) have been proved to improve the photocatalytic activity by controlling the size of the NPs.

Marzun et al. have demonstrated the enhanced photocatalytic water splitting efficiency made by laser ablating palladium nanoparticle in saline solution as a facile route to heterogeneous catalysts [15]. Especially for noble metal NPs, due to the characteristic local surface plasmon resonance (LSPR) effect, they are quite efficient in passing photon energy to electrons in semiconductor [16–18]. Chen has demonstrated an enhanced photocatalytic activity by depositing Au NPs on TiO₂ which is attributed to the intensified electric field at the interface between NPs and semiconductor [19]. Another effect that Au NPs has to enhance the photocatalytic activity is they help to stabilize the electrons and holes [20]. It has been demonstrated that the photocatalytic activity can be tuned by varying the size and shape of the NPs under visible light radiation [21,22], which requires fully size-control of the NPs.

In our previous reports, we deposited gold atoms directly to the STO surface and the NPs are self-assembled on the STO. Although the size of the NPs on STO was not single, the NP/STO exhibited visible light response [23]. Later, noble metal nanoclusters (NCs) was synthesized through gas phase and size selected by a quadrupole mass spectrometer. By decorating the size-selected NCs to STO, visible light response was achieved and the photocurrent was improved [24]. Based on the experimental findings, NP/STO exhibits higher photocatalytic activity than NC/STO, which may be attributed to the LSPR effect for NPs. Due to the strong bonding from STO, NCs and NPs easily deform, which makes the size of NP less controllable. Under this background, a liquid substrate would be a promising candidate for soft-landing of atoms for NP production. On the other hand, the microstructure of the NPs can be tuned by varying deposition conditions such like oil temperature [25]. Comparing with other systems [26,27], nanoparticle synthesis via vaporizing metal atoms to a liquid substrate provides a low cost and flexible method to produce NP co-catalysts. However, the NPs fabricated on a liquid surface commonly appears to be aggregates which mean NPs are highly overlapped [25]. The overlapping behavior of the NPs in the aggregates may bring negative impact on the photocatalytic activity on NPs as co-catalyst. Therefore, the photocatalytic activity may be maximized by fabricating dispersed NPs on a liquid substrate and relevant research is still lacking.

In this research, we have successfully fabricated dispersed silver NPs on a silicone oil surface by lowering the deposition flux. The dispersed NPs are fabricated under varied substrate temperatures. Scanning electron microscopic study demonstrates that no obvious overlapping of NPs occurs and NPs are dispersed on liquid surface under substrate temperature 333 K. By transferring the NPs to a STO surface, the photocatalytic activity of NP/STO is investigated. The relative current density under visible light radiation increases dramatically for NPs fabricated at substrate temperature from 253 K to 333 K. A slight decrease of relative current density is found as substrate temperature further increases to 353 K and the maximum value reaches 25.4 $\mu\text{A}/\text{cm}^2$. Combined with the transmission electron microscopic, atomic force microscopic and incident photon to electron conversion spectrum investigations, we have proposed competition mechanism for NP/STO photocatalyst.

2. Results and Discussion

Figure 1a shows the SEM image of the silver NPs fabricated under substrate temperature of 313 K. It can be seen clearly that NPs are dispersed on the STO surface and no overlapping of NPs is visible, i.e., a single layer of silver NPs are presented. The observation is quite different from previous reports in which NPs usually overlap to form ramified aggregates [25,28]. The size of the NPs are measured and the size histogram of the NP diameter is shown in Figure 1b. The data analysis function in Igor Pro. demonstrates that the mean size for the NPs is 7.8 nm and the standard deviation is 1.0 nm. For statistical purpose, we count NPs from 5 SEM images fabricated under same deposition condition. Comparing with the previous experimental findings, the NP size distribution presented here is quite narrow [25,28]. For comparison purpose, we also present the SEM image (Figure 1c) and corresponding size histogram (Figure 1d) for the same Ag NP/STO photocatalyst after 2 h of photoelectrochemical measurement. It can be seen that most of Ag NPs are still immobilized on STO. Overlapping behavior do occur as indicated in the brighter regions.

The NP size histogram suggests a slight increase of mean size from 7.5 nm to 9.2 nm and standard deviation from 1.0 nm to 1.5 nm, indicating coalescences of NPs may occur during the photoelectrochemical measurement process. The Figure S1 in Supplemental Materials is the XRD spectrum for NP/STO in which peaks corresponding to the STO and Ag can be observed. Carbon peaks are also visible in the spectrum which may due to the methanol or acetone washing. The firm attachment of Ag NPs on STO could be attributed to chemical etching process creates atomic layers which may bond the NPs more tightly.

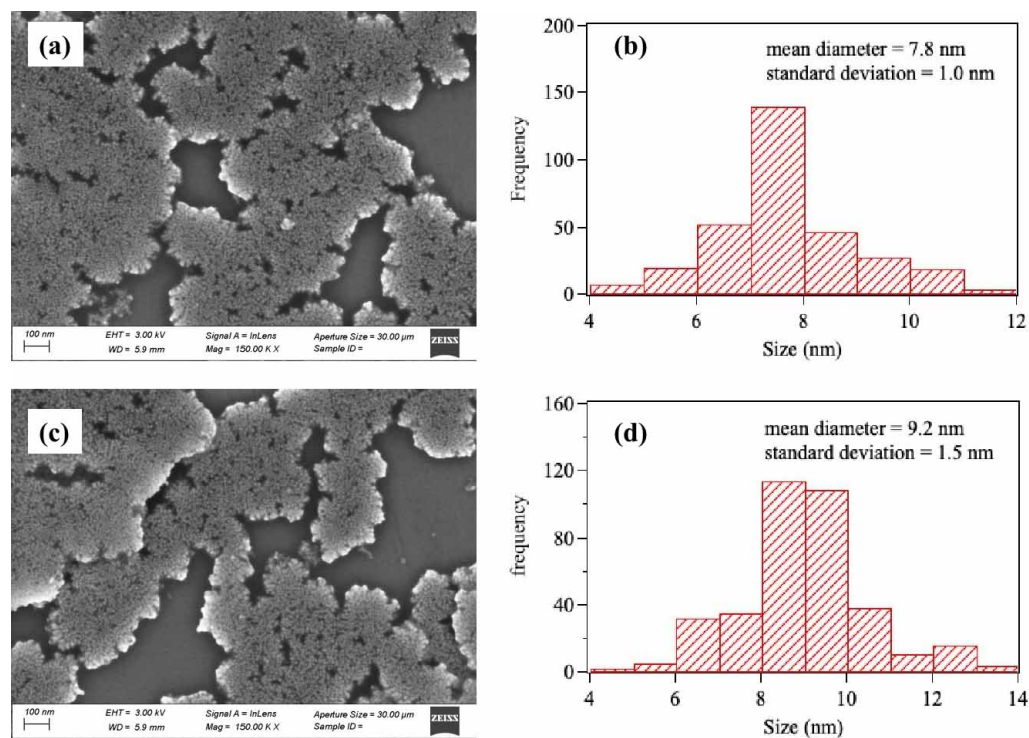


Figure 1. (a) SEM image of Ag NP/STO fabricated under $T = 313$ K. (b) Corresponding size histogram for NPs. (c,d) are SEM image and size histogram for Ag NP/STO after 2 h of photoelectrochemical measurement.

The formation of dispersed NPs shown in Figure 1 may due to the low deposition flux f . It has been demonstrated that when atoms are deposited on the liquid substrate, the diffusion rate is much greater than on the solid substrate, leading to quick formation of NPs [29]. Under normal deposition flux such as $f = 0.1$ nm/s to $f = 1$ nm/s, the silver atoms are deposited quickly to the liquid substrate leading to quick formation of NPs. In this case, the sequential deposition of Ag atoms may land directly on the NPs, leading to formation of Ag aggregates. This may explain the height of the ramified aggregates goes up with the deposition flux [25]. On the other hand, due to the relative weak interaction received from the liquid molecules, NPs become easier to overlap to minimize the total energy. In this research, due to the relatively small $f = 0.001$ nm/s, both the rate of the formation of Ag NPs and the sequential deposition of Ag atoms on the liquid substrate occur slowly. Therefore, the direct deposition of Ag atoms on the NPs will be suppressed. In this case, individual NPs are formed and no obvious overlapping among NPs is observed. The formation of dispersed NPs in this research opens up a way to apply the Ag NPs grown on liquid substrate to areas like microfluidics and photocatalysis.

The photocatalytic activity of the NP/STO sample is investigated by measuring the photocurrent by PEC measurement. Figure 2a (red curve) presents a typical potential-current curve for NP/STO in which the NPs are fabricated under substrate temperature $T = 313$ K. For comparison, the potential-current curve for a bare STO is presented in Figure 2a (blue curve). Pulsed currents are observed under visible light radiation, indicating the NP/STO exhibits visible light response. However, no obvious photo-response is

detected for bare STO which demonstrates that the decoration of Ag NPs enables the visible light response for STO. It should be mentioned that the NPs are immobilized in the STO surface longer than 24 h which is confirmed by the comparison between SEM images of NP/STO within a time interval of 1 day. By subtracting the background current, we obtain the relative current density j_r at potential 0.4 V vs. Ag/AgCl and the dependent behavior of j_r with T is given in Figure 2b. For each NPs, we conduct more than 5 PEC measurements and the error bar is taken as the half range of the j_r . It can be seen that the values of j_r are below $10 \mu\text{A}/\text{cm}^2$ for NPs fabricated under low temperature at $T = 253 \text{ K}$ and 273 K . A dramatic improvement of j_r from $8.4 \mu\text{A}/\text{cm}^2$ to $19.4 \mu\text{A}/\text{cm}^2$ is observed as T rises from 273 K to 293 K . In this research, a maximum value of j_r attained is $25.4 \mu\text{A}/\text{cm}^2$ for $T = 333 \text{ K}$, which is comparable with the value attained in our previous research [23]. However, as T further goes up to 353 K , j_r slightly decreases to $22.8 \mu\text{A}/\text{cm}^2$.

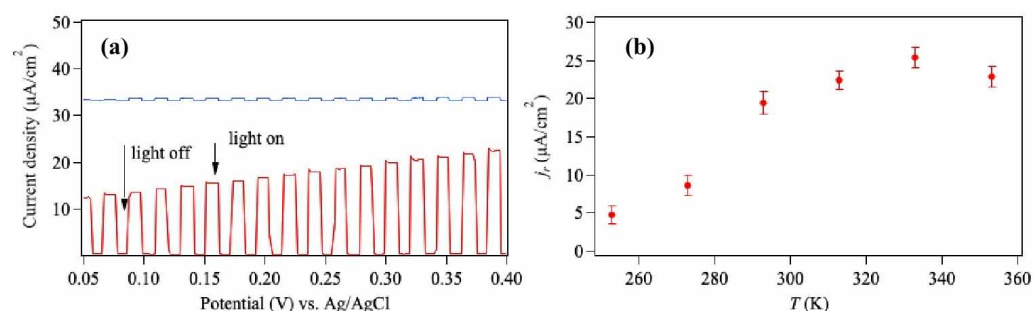


Figure 2. (a) Typical current-potential curves for NP/STO (red) and bare STO (blue). The NPs are synthesized under substrate temperature $T = 313 \text{ K}$. (b) Dependent behavior for the relative current density j_r as a function of the substrate temperature T .

The photocatalytic activity for NP/semiconductor system is determined by the electron separation and transfer rate from semiconductor to NP surface for water splitting [30–32]. Therefore, the crystal structure of the NPs is reported to have great impact on the photocatalytic activity [33]. It has been revealed that the substrate temperature will impact on the microstructure of the NPs [25]. Therefore, we propose that the photocatalytic activity of NP/STO may be influenced by the microstructure of the NPs. Figure 3 show the TEM images for NPs fabricated under varied temperature of 273 K , 293 K , and 333 K . As guided by the white arrows, the NPs fabricated under 273 K shows very weak crystalline structure. The crystal orientations become more obvious when T goes up to 293 K and clear polycrystalline structure can be observed for NPs fabricated under 333 K , as shown in Figure 3c. The above comparison can be supported by the diffraction patterns shown in Figure 3 in which the diffraction rings for Ag NPs in Figure 3b are brighter than those in Figure 3a. The weak crystal orientation in Figure 3a may indicate the presence of more impurities such as oil molecule in the NPs, and in this case, the electron transfer rate from STO to NPs may be lowered. As T increases to 293 K , the NPs exhibit clear crystalline structure and therefore, the electrons are transferred at a faster rate from STO to the hydrogen ions to produce larger current density.

However, the above proposal is unlikely to explain the phenomenon that j_r decreases when T is further increased to 353 K , because higher T usually means better crystal structure and therefore higher j_r . Therefore, the reduction of the j_r for NP fabricated under 353 K may due to a different scheme such as overlapping of NPs that has been reported for NPs grown on liquid substrate. In order to address this anomalous behavior, we utilize the SEM to check the morphology of the NPs fabricated under 353 K . Figure 4a is SEM image for the NPs fabricated under 353 K , in which clear overlapping among NPs can be seen (white circles). Meanwhile, comparing with the SEM images shown in Figure 1a, the overall surface coverage of the NPs is smaller for Figure 4a. We attribute this morphological change to the increased kinetic energy of the Ag atoms due to higher substrate temperature

because the growth model of Ag NPs tends to obey a 3D growth, which is consistent with our previous finding [25].

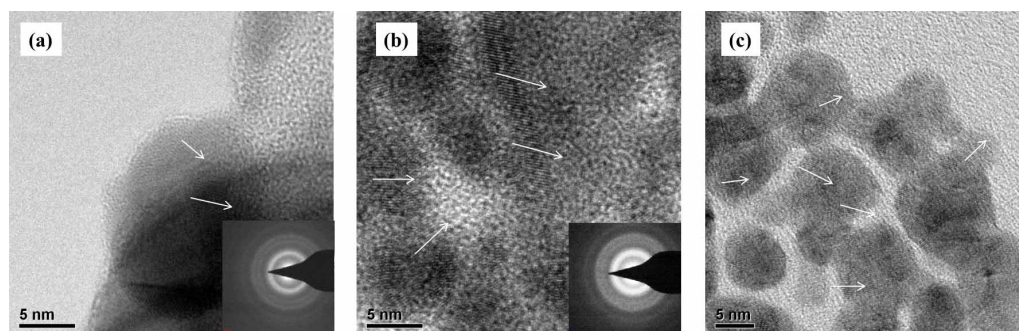


Figure 3. Transmission electron microscopic images for NPs fabricated under $T =$ (a) 273 K, (b) 293 K and (c) 333 K. White arrows indicate the different crystal orientations. The diffraction patterns indicates the ploy-crystalline structure of the NPs.

The line profile presented by the atomic force microscopic (AFM) gives a straight forward way to visualize the NP overlapping behavior. Figure 4b shows an AFM image for NPs fabricated under $T = 353$ K. The dark area represents the positions with smaller height while the bright areas show the higher positions. We can see Ag NPs are distributed on the surface of STO, which is consistent with the SEM images. Figure 4c is the line profile of the white line marked in Figure 4b and the length of the line is 400 nm as shown in the figure. At the position around 100 nm, there is a clear step resulting from the overlap of NPs. It can also be estimated that the height of the NPs are around 1–2 nm, indicating the geometrical shape of the NPs is near an ‘egg’.

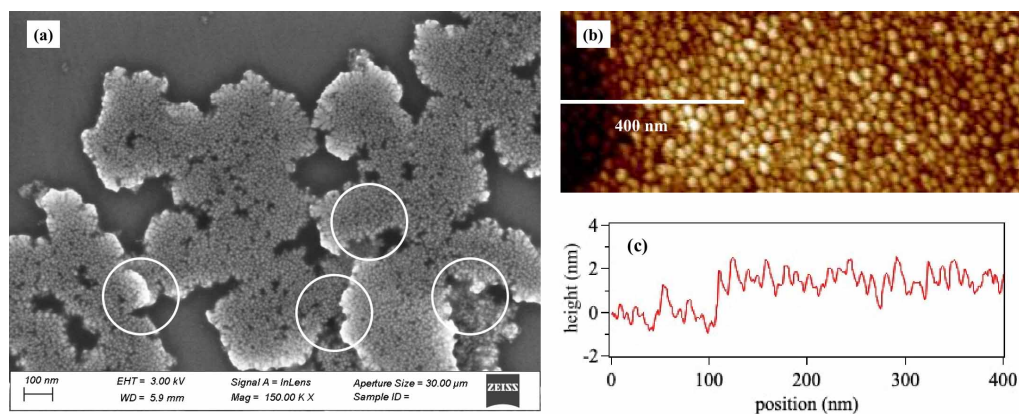


Figure 4. (a) Scanning electron microscopic image for NPs fabricated under 353 K. White circles indicates clear overlapping of NPs. (b) Atomic force microscopic image for NPs. (c) Line profile of the white line marked in (b).

In order to obtain a quantitative evidence for the above proposal, we calculate the apparent surface coverage ρ of the Ag NPs and the dependent manner of ρ and substrate temperature T is presented in Figure 5a. The value of ρ is calculated by using 5 SEM images for each sample and the errors are determined by taking the half value of the range of ρ . It can be found that the value of ρ maintains around 70% under $T = 313$ K, indicating the growth behavior of the Ag NPs is not dramatically influence by T . As T further increases to 333 K, the value of ρ starts to decrease to around 60%, which may mainly due to the elimination of impurities in the NPs and therefore NPs start to show better crystalline structure. As T further increases from 333 K to 353 K, a dramatic reduction of ρ from 58.3% to 40.5% can be seen, indicating the growth model of NPs begins to vary and NPs start to overlap. The main reason for the reduced surface coverage under higher substrate temperature may due to two reasons: the deposited Ag atoms gain more energy to form a

more spherical NPs to minimize the total energy of the NPs and the weakened interaction from the liquid molecules on the NPs causes the 3D growth of the NPs. As a result, the effective contact area between NPs and STO is reduced, which may cause a slower charge transfer from STO to NPs.

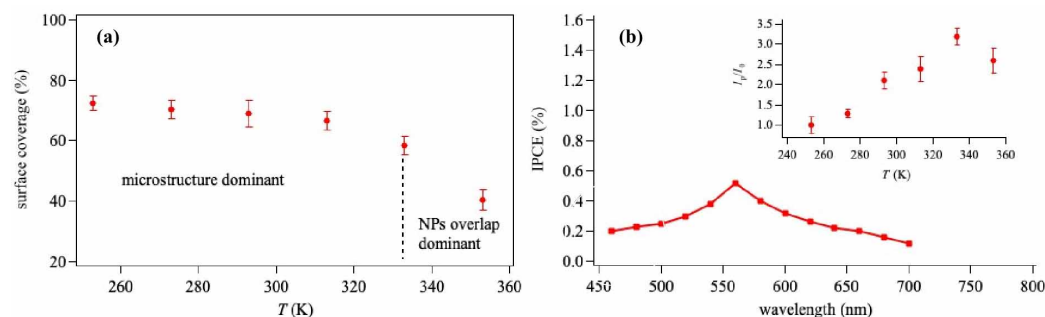


Figure 5. (a) Dependence between surface coverage of NPs (ρ) and substrate temperature (T). The dashed lines represent the different mechanisms that dominate the photocatalytic activity under varied T . (b) IPCE spectrum for NPs fabricated under 313 K. Dependency between the relative intensity of IPCE spectra and T is shown as an inset.

The charge transfer rate can qualitatively demonstrated by the incident photon to current conversion efficiency (IPCE) spectra. Figure 5b is a typical IPCE spectrum for the NP which is fabricated under $T = 313$ K. A clear absorption peak can be found around the wavelength of 560 nm, mirroring the charge separation occur on the NP-STO surface initiate by the visible light radiation. By counting the relative intensity of the peak value (I) in the IPCE spectra and set $I_0 = 1$ for NPs fabricated under $T = 253$ K, the relative spectrum intensity I/I_0 is calculated and shown in the inset of Figure 5b. It can be found that the value of I/I_0 gradually increases from 1.0 to 3.2 as T goes up from 253 K to 333 K. A decrease manner of I/I_0 from 3.2 to 2.6 is observed as T further increases from 333 K to 353 K. The observation in IPCE spectrum is quite consistent with the dependent behavior of relative current density j_r and T which is shown in Figure 2b, indicating the increased relative current density for 253 K to 333 K is actually due to the faster charge transfer rate at higher temperature. The decreasing of relative current density for 353 K is mainly because of overlap of NPs under this temperature would decrease the efficient contact area between NPs and STO, leading to a slower charge transfer rate.

Based on the above observations, we are able to propose a mechanism for the water splitting on the Ag NP/STO system. For NPs fabricated under relatively low temperature (≤ 313 K), impurities such as oil molecule are more likely to be integrated to the NPs. As a result, the crystalline structure of NPs are less obvious and therefore the charge transfer rate from STO to NPs would be slowed down, leading to relatively low relative current density. As T increases from 313 K to 333 K, the deposited atoms gains more energy to form NPs with higher crystalline structure and the number of impurities in NPs is dramatically reduced which can be reflected by an improved crystalline structure seen in TEM image and the diffraction pattern. In this case, the charge transfer rate from STO to NPs are enhanced causing a increased relative current density. Although the surface coverage evolution suggests that overlap manner among NPs may take place at $T = 333$ K which is a negative impact to the relative current density, the improvement of crystalline structure is the dominant factor. Therefore, the relative current density reaches a maximum value of $25.4 \mu\text{A}/\text{cm}^{-2}$, as indicated in Figure 5a. However, as T further increases to 353 K, although NPs exhibit even better crystalline structure, the relative current density is mainly influenced by the overlap behavior of NPs. The overlapping behavior of the NPs will increases the diffusion distance of the electrons from STO to NP surface, which in turn reduces the electrons transfer rate. On the other hand, overlapping of NPs reduces the amount of NPs that are in direct contact with the STO leading to a slower electron transfer

efficiency. In this case, the relative current density shows a slight decrease when T increases from 333 K to 353 K.

3. Materials and Methods

The silver nanoparticles were prepared by thermal vaporization method in a vacuum chamber with background pressure of 0.1 Pa. Silver wires (99.99% pure, Goodfellow, Shanghai, China) were hang on a filament wire which was biased by a variable voltage. The substrate was prepared by painting a thin layer of silicone oil (Dow Corning 705 Diffusion Pump Fluid) on a clean frosted glass surface, resulting in a thin oil film of around 1 mm thickness. When the applied voltage on the filament exceeded a certain value, Ag wires melted and Ag atoms were deposited onto substrate, as shown in Figure 6. The substrate (frosted glass and oil) temperature can be adjusted by a self-designed semiconductor temperature control unit which was kept right beneath the substrate so that the temperature of the substrate can be tuned from 250 K to 370 K. Before deposition, the substrate was kept under a movable shield and the shield was removed when the deposition began. It should be mentioned that the temperature control unit was kept under a certain temperature so that heat from the control unit would efficiently conducted to the substrate to ensure that the temperature of the substrate was the same as the control unit. The deposition flux f and amount (nominal film thickness d) were monitored by a quartz balance (CRTM 8000). In order to fabricate dispersed NPs instead of aggregates, we used low deposition flux at $f = 0.001$ nm/s and in this research, the nominal film thickness d was 5 nm.

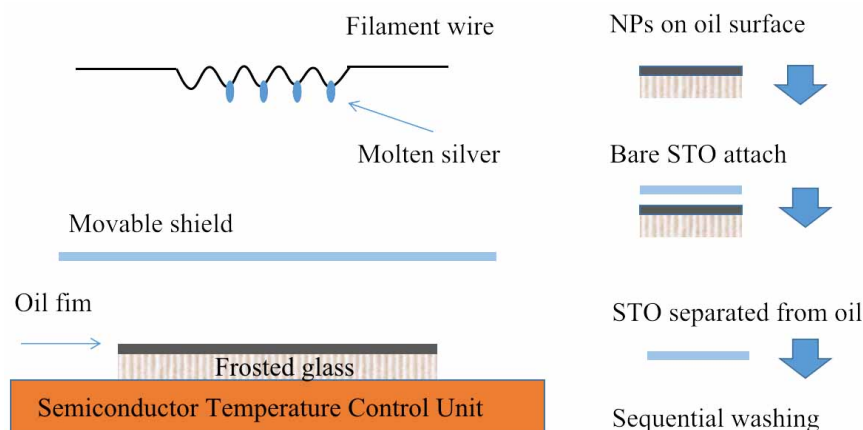


Figure 6. Illustrative sketch of the experimental apparatus. The separation process of NPs from oil surface to a clean STO is also indicated.

After deposition, the sample was kept under vacuum condition for 0.5 h before removing from the vacuum chamber. During this period, a strontium titanate crystal (STO, MTI Co., Inc., Richmond, CA, USA) was pre-etched by a mixed solution of hydrofluoric acid (HF, 3 mL) and ammonium fluoride (NH_4F , 7 mL) so that organic contaminations would be cleaned. On the other hand, the atomic layers on an etched STO could play a role on stabilizing NPs [34]. After that, the STO was gently placed on the sample surface and the Ag NPs on the liquid surface were attached firmly to the STO surface. The STO was then removed from the sample surface and a sequential washing by acetone and methanol was performed on the STO to remove the oil on the surface. This unique NP separation and washing process have been frequently adapted in previous work because NPs are highly stable on the crystal surface for days [35–38]. After washing, the NP/STO system was pumped in the vacuum chamber for 0.5 h. The NP/STO sample was then kept in a container which was initially pumped and transferred to scanning electron microscopic (ZEISS SUPRA 55 SAPPHIRE, Carl Zeiss, Shanghai, China) study. The SEM observations were conducted under an accelerating potentials of 3 kV to avoid heating effect by energetic electron beams. For each NP/STO system, we performed SEM measurements on different locations for several times. For atomic force microscopic (AFM, Nano DI 3000, Veeco

Inc. USA) study, we utilize an ambient tapping mode with a scan rate of 1 Hz. The line profile of the AFM image was proceeded by the Nanoscope Analysis software. The size of the NPs were measured by a self-designed measuring software and analyzed by an Igor Pro. 9 software. For transmission electron microscopic (TEM, JEM2010) investigations, an amorphous carbon mesh was placed gently on the sample surface to transfer NPs from oil surface to the mesh. The mesh with NPs were then washed by acetone and methanol to remove the oil contaminations. For X-ray diffraction measurement, a Rigaku Miniflex X-ray diffractometer was used with scanning speed of $2\theta = 2^\circ/\text{min}$ with a step size of 0.02° .

In order to evaluate the photocatalytic activity of the NP/STO, we used a photoelectrochemical cell (PEC) which was composed of a pyrex glass container, a drum-shaped anode for loading of NP/STO, a platinum wire as cathode, a reference electrode of Ag/AgCl. We utilized Na_2SO_4 solution at a concentration of 0.02 M. The drum-shaped electrode was made of Teflon insulator with a quartz window in front of it so that the NP/STO catalyst would have an apparent radius of 0.5 cm exposed to the light source [24]. For the visible light radiation, we adapted pulsed light (300 W Xe lamp (Asahi Spectra. MX-303, Torrance, CA, USA) coupled with a AM 1.5 filter) with each on time duration of 1.0 s. In this experiment, the scan rate of the potentiostat was 10 mV/s and the potential-current curve was recorded by the potentiostat.

For calculation of the apparent coverage of NPs, we wrote a script (M-file) based on a Matlab program. The SEM image was first imported by the script automatically to the Matlab program and then converted to a greyscale image. The background of the image was then subtracted from the grayscale image before it was transferred to a two dimensional pixel matrix with total number of element N . In order to determine the minimum pixel value that is representing NPs, we used the following algorithm: an initial threshold pixel value was set to represent NP and then the surface coverage was calculated. After that, the threshold pixel value was automatically increased by 1 and the surface coverage was calculated again and then the difference between the value of two surface coverages were calculated. The above proceed continued until the difference between values was below a threshold. In this case, the threshold pixel value was determined. The pixel values in the pixel matrix were compared with the threshold pixel value and the number of values (N_1) that is higher than the threshold was recorded. The surface coverage of the NPs on STO was then calculated as N_1/N .

4. Conclusions

We have successfully synthesized the dispersed Ag NPs by utilizing a small deposition flux on a liquid substrate under varied substrate temperature and then transferred the Ag NPs to a strontium titanate crystal (STO). The transmission electron microscopic investigation has demonstrated that the crystalline structure of NPs is improved when substrate temperature increases. The PEC measurement on the NP/STO system indicates the photocatalytic activity of NP/STO system is enhanced when T increases from 253 K to 333 K, which is mainly attributed to the improved crystalline structure of the NPs. The maximum relative current density j_r in this research reaches $25.4 \mu\text{A}/\text{cm}^2$. As T further increases to 353 K, the reduced j_r is attributed to the change of the growth model of NPs: (1) NPs start to overlap which reduces the apparent contact area between NPs and STO; (2) diffusion distance of electrons from STO to NP surface is increased leading to a reduced charge transfer efficiency from STO to NP surface. The above proposal is supported by the IPCE observation in which the relative intensity of the spectrum peak gradually increases with T from 253 K to 333 K and then slightly decrease when T is 353 K.

Supplementary Materials: The following supporting information can be downloaded at: <https://www.mdpi.com/article/10.3390/catal13060946/s1>, Figure S1: XRD spectrum for Ag NP/STO. JCPDS card numbers for STO (00-040-1500) and AgNPS (00-004-0783). Figure S2: The relative current density (j_r) varies with deposition nominal film thickness (d). Deposition flux $f = 0.001$ nm/s and substrate temperature $T = 293$ K.

Funding: This research received no external funding.

Data Availability Statement: Not applicable.

Acknowledgments: The author appreciates the SEM imaging support from Quanlin Ye in physics department of Hangzhou Normal University and useful discussion from Ziran Ye from Zhejiang University of Technology. SEM measurement by Liwei Yu and Hongrui Pu from Hangzhou Wickham International School are also acknowledged.

Conflicts of Interest: The authors declare no conflict of interest.

References

1. Fujishima, A.; Honda, K. Electrochemical Photolysis of Water at a Semiconductor Electrode. *Nature* **1972**, *238*, 37–38. [[CrossRef](#)] [[PubMed](#)]
2. Mills, A.; LeHunte, S. An overview of semiconductor photocatalysis. *J. Photochem. Photobiol. A* **1997**, *108*, 1–35. [[CrossRef](#)]
3. Ohno, T.; Mitsui, T.; Matsumura, M. Photocatalytic activity of S-doped TiO₂ photocatalyst under visible light. *Chem. Lett.* **2003**, *32*, 364–365. [[CrossRef](#)]
4. Hamann, T. Perovskites take lead in solar hydrogen race. *Science* **2014**, *345*, 1566–1567. [[CrossRef](#)] [[PubMed](#)]
5. Joy, R.; Haridas, S. Strontium titanate aided water splitting: An overview of current scenario. *Int. J. Hydrogen Energy* **2021**, *46*, 1879–1903. [[CrossRef](#)]
6. Iwashina, K.; Kudo, A. Rh-Doped SrTiO₃ Photocatalyst Electrode Showing Cathodic Photocurrent for Water Splitting under Visible-Light Irradiation. *J. Am. Chem. Soc.* **2011**, *133*, 13272–13275. [[CrossRef](#)]
7. Maeda, K. Rhodium-Doped Barium Titanate Perovskite as a Stable p-Type Semiconductor Photocatalyst for Hydrogen Evolution under Visible Light. *ACS Appl. Mater. Interfaces* **2014**, *6*, 2167–2173. [[CrossRef](#)]
8. Kiyonaga, T.; Fuji, M.; Akita, T.; Kobayashi, H.; Tada, H. Size-dependence of Fermi energy of gold nanoparticles loaded on titanium(IV) dioxide at photostationary state. *Phys. Chem. Chem. Phys.* **2008**, *10*, 6553–6561. [[CrossRef](#)]
9. Berr, M.J.; Schweinberger, F.F.; Dobliger, M.; Sanwald, K.E.; Wolff, C.; Breimeirer, J.; Crampton, A.S.; Ridge, C.J.; Tschurl, M.; Heiz, U.; et al. Size-Selected Subnanometer Cluster Catalysts on Semiconductor Nanocrystal Films for Atomic Scale Insight into Photocatalysis. *Nano Lett.* **2012**, *12*, 5903–5906. [[CrossRef](#)]
10. Zhao, W.; Bai, Z.; Ren, A.; Guo, B.; Wu, C. Sunlight photocatalytic activity of CdS modified TiO₂ loaded on activated carbon fibers. *Appl. Surf. Sci.* **2010**, *25*, 3493–3498. [[CrossRef](#)]
11. Qian, K.; Sweeny, B.C.; Johnson-Peck, A.C.; Niu, W.; Graham, J.O.; DuChene, J.S.; Qiu, J.J.; Wang, Y.; Engelhard, M.; Su, D.; et al. Surface Plasmon-Driven Water Reduction: Gold Nanoparticle Size Matters. *J. Am. Chem. Soc.* **2014**, *136*, 9842–9845. [[CrossRef](#)]
12. Li, S.; Miao, P.; Zhang, Y.; Wu, J.; Zhang, B.; Du, Y.; Han, X.; Han, J.; Sun, J.; Xu, P. Recent Advances in Plasmonic Nanostructures for Enhanced Photocatalysis and Electrocatalysis. *Adv. Mater.* **2021**, *33*, 2000086. [[CrossRef](#)] [[PubMed](#)]
13. Moniruddin, M.; Afroz, K.; Shabdan, Y.; Bizri, B.; Nuraje, N. Hierarchically 3D assembled strontium titanate nanomaterials for water splitting application. *Appl. Surf. Sci.* **2017**, *419*, 886–892. [[CrossRef](#)]
14. Amer, M.S.; Arunachalam, P.; Al-Mayouf, A.M.; Prasad, S.; Alshalwi, M.N.; Ghanem, M.A. Mesoporous Tungsten Trioxide Photoanodes Modified with Nitrogen-Doped Carbon Quantum Dots for Enhanced Oxygen Evolution Photo-Reaction. *Nanomaterials* **2019**, *9*, 1502. [[CrossRef](#)]
15. Marzun, G.; Nakamura, J.; Zhang, X.; Barcikowski, S.; Wagener, P. Size control and supporting of palladium nanoparticles made by laser ablation in saline solution as a facile route to heterogeneous catalysts. *Appl. Surf. Sci.* **2015**, *348*, 75–84. [[CrossRef](#)]
16. Yoo, S.; Rawal, S.; Lee, J.; Kim, J.; Ryu, H.; Park, D.; Lee, W. Size-dependence of plasmonic Au nanoparticles in photocatalytic behavior of Au/TiO₂ and Au@SiO₂/TiO₂. *Appl. Catal. A-Gen.* **2015**, *499*, 47–54. [[CrossRef](#)]
17. Liu, S.; Xu, Y. Photo-induced transformation process at gold clusters-semiconductor interface: Implications for the complexity of gold clusters-based photocatalysis. *Sci. Rep.* **2016**, *6*, 22742. [[CrossRef](#)] [[PubMed](#)]
18. Weng, B.; Jiang, Y.; Liao, H.; Lai, F.; Huang, H.; Tang, Z. Visualizing light-induced dynamic structural transformations of Au clusters-based photocatalyst via in situ TEM. *Nano Res.* **2021**, *14*, 2805–2809. [[CrossRef](#)]
19. Chen, J.; Wu, J.; Wu, P.; Tsai, D. Plasmonic Photocatalyst for H₂ Evolution in Photocatalytic Water Splitting. *J. Phys. Chem. C* **2011**, *115*, 210–216. [[CrossRef](#)]
20. Priebe, B.; Radnik, J.; Lennox, J.; Pohl, M.; Karnahl, M.; Hollmann, D.; Grabow, K.; Bentrup, U.; Junge, H.; Beller, M.; et al. Solar Hydrogen Production by Plasmonic Au-TiO₂ Catalysts: Impact of Synthesis Protocol and TiO₂ Phase on Charge Transfer Efficiency and H₂ Evolution Rates. *ACS Catal.* **2015**, *5*, 2134–2148. [[CrossRef](#)]
21. Zaleska-Medynska, A.; Marchelek, M.; Diak, M.; Grabowska, E. Noble metal-based bimetallic nanoparticles: The effect of the structure on the optical, catalytic and photocatalytic properties. *Adv. Colloid Interface* **2016**, *229*, 80–107. [[CrossRef](#)]

22. Kumar, A.; Choudhary, P.; Kumar, A.; Camargo, P.H.C.; Krishnan, V. Recent advances in plasmonic photocatalysis based on TiO₂ and noble metal nanoparticles for energy conversion, environmental remediation, and organic synthesis. *Small* **2022**, *18*, 2101638. [[CrossRef](#)] [[PubMed](#)]
23. Zhang, C.; Feng, Y. Self-Assembled Gold Nanoparticles on Strontium Titanate for Efficient Photocatalytic Water Oxidization and Visible Light Response. *Mater. Res. Express* **2015**, *2*, 095021. [[CrossRef](#)]
24. Zhang, C. Deposition of Size-Selected Gold Nanoclusters onto Strontium Titanate Crystals for Water Splitting under Visible Light. *Catalysts* **2022**, *12*, 367. [[CrossRef](#)]
25. Zhang, C.; Lv, N.; Zhang, X.; Yang, B.; Ye, G. Preferred structures of the atomic Ag islands on silicone oil surfaces. *J. Phys. Condens. Matter* **2011**, *23*, 435006 [[CrossRef](#)]
26. Phoon, B.L.; Lai, C.W.; Pan, G.T.; Yang, T.C.K.; Juan, J.C. One-pot hydrothermal synthesis of strontium titanate nanoparticles photoelectrode using electrophoretic deposition for enhancing photoelectrochemical water splitting. *Ceram. Int.* **2012**, *44*, 9923–9933. [[CrossRef](#)]
27. Amer, M.; Arunachalam, P.; Ghanem, M.A.; Abdullah, A.M.; Weller, M.T. Photoelectrochemical Performance of Strontium Titanium Oxynitride Photo-Activated with Cobalt Phosphate Nanoparticles for Oxidation of Alkaline Water. *Nanomaterials* **2023**, *13*, 920. [[CrossRef](#)]
28. Zhang, C.; Lv, N.; Zhang, X.; Ye, G. Anomalous Kinetic Roughening of Nanostructured Ag Islands on Liquid Surfaces. *J. Phys. Soc. Jpn.* **2012**, *81*, 034602. [[CrossRef](#)]
29. Ye, G.; Michely, T.; Weidenhof, V.; Friedrich, I.; Wuttig, M. Nucleation, Growth, and Aggregation of Ag Clusters on Liquid Surfaces. *Phys. Rev. Lett.* **1996**, *81*, 622. [[CrossRef](#)]
30. Bunker, C.E.; Smith, M.J. Nanoparticles for hydrogen generation. *J. Mater. Chem.* **2011**, *21*, 12173–12180. [[CrossRef](#)]
31. Wang, Q.; Hisatomi, T.; Jia, Q.; Tokudome, H.; Zhong, M.; Wang, C.; Pan, Z.; Takata, T.; Nakabashi, M.; Shibata, N.; et al. Scalable water splitting on particulate photocatalyst sheets with a solar-to-hydrogen energy conversion efficiency exceeding 1%. *Nat. Mat.* **2016**, *15*, 611–615. [[CrossRef](#)]
32. Fang, M.; Tan, X.; Liu, Z.; Hu, B.; Wang, X. Recent Progress on Metal-Enhanced Photocatalysis: A Review on the Mechanism. *Research* **2021**, *2021*, 9794329. [[CrossRef](#)] [[PubMed](#)]
33. Yang, L.; Zhou, H.; Fan, T.; Zhang, D. Semiconductor photocatalysts for water oxidation: Current status and challenges. *Phys. Chem. Chem. Phys.* **2014**, *16*, 6810–6826. [[CrossRef](#)] [[PubMed](#)]
34. Kawasaki, M.; Takahashi, K.; Maeda, T.; Tsuchiya, R.; Shinohara, M.; Ishiyama, O.; Yonezawa, T.; Yoshimoto, M.; Koinuma, H. Atomic Control of the SrTiO₃ Crystal Surface. *Science* **1994**, *166*, 1540–1542. [[CrossRef](#)]
35. Lu, C.X.; Cheng, Y.; Pan, Q.F.; Tao, X.M.; Yang, B.; Ye, G.X. One-dimensional Growth of Zinc Crystals on a Liquid Surface. *Sci. Rep.* **2016**, *6*, 19870. [[CrossRef](#)]
36. Lu, C.X.; Jin, Y.; Tao, X.M.; Yang, B.; Ye, G.X. Nucleation and growth of zinc crystals on a liquid surface. *CrystEngComm* **2018**, *20*, 122–127. [[CrossRef](#)]
37. Ye, Z.R.; Huang, H.X.; Xu, F.Y.; Lu, P.; Chen, Y.B.; Shen, J.W.; Ye, G.X.; Gao, F.; Yan, B. Surface enhanced Raman scattering substrates prepared by thermal evaporation on liquid surfaces. *Nanotechnology* **2018**, *29*, 375502. [[CrossRef](#)]
38. Ye, Z.R.; Sun, G.F.; Sui, C.H.; Yan, B.; Gao, F.; Cai, P.G.; Lv, B.; Li, Y.; Chen, N.B.; Xu, F.Y.; et al. Thermal Annealing Effect on Surface-Enhanced Raman Scattering of Gold Films Deposited on Liquid Substrates. *Molecules* **2023**, *28*, 1472. [[CrossRef](#)]

Disclaimer/Publisher's Note: The statements, opinions and data contained in all publications are solely those of the individual author(s) and contributor(s) and not of MDPI and/or the editor(s). MDPI and/or the editor(s) disclaim responsibility for any injury to people or property resulting from any ideas, methods, instructions or products referred to in the content.